JOURNAL OF SOLID STATE CHEMISTRY 91, 82–97 (1991)

Anisotropy of Thermal Expansion of the Brannerite-Type MnV_2O_6: Effect of Doping with MoO_3 and Li_2O; Theoretical Predictions, Verification, New Rules

WALDEMAR BOBIŃSKI AND JACEK ZIÓŁKOWSKI*

Institute of Catalysis and Surface Chemistry, Polish Academy of Sciences, 30-239 Kraków, ul. Niezapominajek, Poland

Received June 4, 1990; in revised form October 19, 1990

Thermal expansion of the brannerite-type phases has been studied with the high temperature X-ray diffraction between room-temperature and the decomposition temperatures of 535–660°C. The studies involved the MnLi = $Mn_{1-y}Li_yV_{2-y}Mo_yO_6$ ($0 \leq y \leq 1$) solid solutions, including the lateral compounds MnV_2O_6 and $LiVMoO_6$ and the MnLiϕ = $Mn_{1-x-y}\phi_xLi_yV_{2-2x-y}Mo_{2x+y}O_6$ (x_{max} between 0.16 and 0.45) solid solutions in which Mo^{6+} ions are substituted randomly for V^{5+} and similarly Li^{1+} and cation vacancies ϕ for Mn^{2+}. The results were processes with a number of computer programs and the coefficients of linear thermal expansion $d_{11} > d_{33} \geq d_{22}$ along the main orthogonal X, Y, Z axes have been determined. Y coincides with the crystallographic [010] axis, X lies in the (010) plane and makes an angle α_x with the crystallographic [100] of 54–82°C, depending on the temperature and composition. The values of d_{ii} are between 0.2×10^{-5} and 7.5×10^{-5}. On the assumption of the energy equipartition and using the bond-length–bond-energy concept some predictions concerning the anisotropy of the thermal expansion and the isomorphous substitution effect have been formulated and compared with the experimental data. On this basis the ancient empirical rule that the highest dilatation of a crystal corresponds to a direction of the longest bonds has been replaced with a number of more precise rules including (i) the thermal bond-sensitivity rule (increment $\Delta R\%$ of the bond length corresponding to a given increment of the bond energy Δe is taken as a measure of the bond sensitivity), (ii) the isomorphous substitution rule, (iii) the weak link rule, (iv) the strong chain rule, and (v) the clathrate rule. A comparison of the presently proposed model of thermal expansion and the classical approaches is offered. © 1991 Academic Press, Inc.

1. Introduction

1.1. Physical Description of Thermal Expansion

Attractive and repulsive interactions between the atoms (ions) in a crystal give rise to potential energy wells with a number of allowed vibration levels inside. The higher the temperature, the higher the vibration levels occupied. The mean position of an atom vibrating in a well is given by the middle between the well's walls on the respective level. The atomic positions determine the average distance of the neighboring atoms usually called the bond length (R or $\bar{r}$ in our and classical approaches, respectively). Structure analysis with, e.g., X-ray diffraction, gives mean positions of atoms

* To whom all correspondence should be addressed.

0022-4596/91 $3.00

Copyright © 1991 by Academic Press, Inc.
All rights of reproduction in any form reserved.

and R's ($\bar{r}$'s) for a given crystal. Asymmetry of the attractive and repulsive forces, resulting in the asymmetry of the wells and in an anharmonicity of the lattice vibrations gives rise to the phenomenon of thermal expansion of bonds, which accounts for an expansion of a crystal as a whole. The latter must be a uniform deformation with conservation of the symmetry, as required by Neumann's rule. In crystals of a lower symmetry and a complex chemical composition the wells and their spacial distribution can be differentiated, which accounts for the anisotropy of thermal expansion also involving the angular bond–bond changes. Although a qualitative description of the thermal expansion seems to be easy, a rigorous physical theory of this phenomenon is difficult to formulate (*1, 2*). This is due to the ambiguity of the potential functions and numerical coefficients entering the respective equations to be used and some simplistic assumptions which are still unavoidable.

As an example let us recall, e.g., after (3), that a chemical bond may be considered as a mechanical anharmonic oscillator with damping. Its potential is given by the equation

$$U(x) = ax^2 - bx^3 - cx^4, \qquad (1)$$

where x is a deflection from the equilibrium position r_0 at $T = 0°K$ (where the bond energy is U_0) and $a, b, c > 0$ are the constants of elasticity, anharmonicity, and damping, respectively. The average deflection $\bar{x}$ (used further in Eq. (4)) as a function of temperature T is

$$\bar{x} = \frac{3bkT}{4a^2 + 3ckT}. \qquad (2)$$

As frequently done for the ionic crystals, let us assume that the real potential of interactions between adjacent ions is composed of the coulombic-type attraction and Born-type repulsion,

$$U(r) = -\frac{A}{r} + \frac{B}{r^m}, \qquad (3)$$

where r is the interatomic distance and

$$\bar{r}(T) = r_0 + \bar{x}(T). \qquad (4)$$

Combining the above equations with the definition of a coefficient of linear thermal expansion,

$$d = \frac{1}{r(T)} \frac{\delta r(T)}{\delta T}, \qquad (5)$$

we obtain for d of a bond

$$d = \frac{(m+4) A r_0}{2(m-1)(A - wr_0kT)^2}, \qquad (6)$$

where

$$w = \frac{m^2 + 7m + 18}{8(m-1)}, \qquad (7)$$

and thus

$$d = \frac{32 m (m+4) U_0}{[8 m U_0 - (m^2 + 7m + 18) kT]^2}. \qquad (8)$$

Functions $d(T,r_0)$ and $d(T,U_0)$ (Eqs. (6) and (8)) increase in the allowed range. This means that the larger the initial r_0 or U_0 of the considered cation–anion bond the larger its d. Comparison of d's of the chemically different cation–anion pairs requires, however, the knowledge of coefficients A and m, which cannot be theoretically predicted and which are hardly accessible experimentally. For the strictly ionic crystals (which perhaps do not exist at all in nature, although some come close) A should be equal to the Madelung constant, but m changes markedly even among crystals of the same structure and high chemical affinity (e.g., halides of the NaCl-type). Therefore, the practical use and the "predictive power" of Eqs. (6) and (8) are very limited. The analogous problems arise if potential functions other than those of the Born-type are used (e.g., Born-Mayer, Morse, Lennard-Jones, etc.).

As an alternative to the classical methods we intend to propose in this work an approach which bypasses the above indicated troubles.

1.2. Phenomenological Description of Thermal Expansion

A phenomenological approach may be offered as an alternative to a physical theory, which is also approximate but perhaps more visual and impressive. It can be based on the observations formulated already in the early works on thermal expansion. It has been stated that in anisotropic crystals the highest dilatation corresponds to the direction of the longest (the weakest) bonds. These observations can be now rationalized not only with Eq. (6) but also in terms of the bond-length–bond-strength–bond-energy concept (*4–9*), valid for iono-covalent crystals and developed in particular for oxides.

Bond strength s was defined by Pauling (*4*) as a valence of cation z divided by its coordination k:

$$s = \frac{z}{k}. \tag{9}$$

As reviewed by Brown (*5, 6*), it has been stated later that s must depend on the bond length R. A number of empirical methods for calculating s (vu = valence units) as a function of R (Å) have been proposed so far, two of which having become widely applicable and accepted: the inverse power function

$$s = \left(\frac{R_1}{R}\right)^N \tag{10}$$

and the exponential function

$$s = \exp\left(\frac{R - R_0}{B}\right), \tag{11}$$

where R_1, N, and B are empirical parameters determined for numerous ions making bonds to oxygen, halides, nitrogen, or carbon.

Recently (*7–9*) we have proposed a new coulombic-type equation for the same purpose and we extended the empirical relationship to the atomization enthalpy of a cation–oxygen bond e (kcal mol^{-1})

$$s = \frac{dz}{R - R_0}, \tag{12}$$

$$e = Js, \tag{13}$$

where d (Å) and R_0 (Å) are empirical parameters (related by simple formulas to the standard radii of free ions (*7*) which, by definition, are structure- and temperature-independent) and J (kcal mol^{-1} vu^{-1}) is the standard molar atomization enthalpy of a simple oxide of the considered cation per its valence unit. The above coefficients are listed in the quoted papers for over 200 cations forming bonds with oxygen.

It seems relevant to note that neither Eqs. (10) and (11) nor two empirical parameters they contain have any precise physical meaning, although the equations aim at reflecting the core electron repulsions. On the contrary, Eq. (12) has been deduced from the properties of the ionic radii compiled by Shannon (*10*) (and slightly modified in (*7*)) and contains only one parameter, the radius of a free cation, which has a defined physical meaning. A coulombic-type form of Eq. (12) has been rationalized in the hover model of crystal structure (*7*) and accounts for the most important component of interatomic interactions in crystals. Calculating e from s (Eq. (13)) requires a knowledge of the values of J which either can be found in thermochemical tables (cf. Ref. (*8*)) or calculated (*9*) from the equation

$$J_m = J_n \sqrt{n/m}, \tag{14}$$

where m and n are two different valence states of a given cation.

The R–s and R–s–e relationships have been used for a long time by crystallographers and chemists for such purposes as verification of the determined structures, identification of atoms of different valence states that have similar X-ray scattering factors, localization of light atoms, interpretation of the asymmetry of hydrogen bonds, determination of the active surface energy

of solids, and interpretation of the mechanism of catalytic processes (*5, 6, 11–13*).

The phenomenon of thermal expansion can also be rationalized making use of the *R–s–e* concept in the following way. The crystal lattice may be considered as a tridimensional network of chemical bonds of differentiated energies. On heating the crystal by ΔT, the energy of the lattice increases by $\Delta E = \bar{C}_p \Delta T$. We can assume that to a first approximation we deal with the equipartition of the energy increment ΔE among all the bonds. As the dependence of the bond energy e (or the bond strength s) on the bond length is hyperbolic (Eqs. (10–13), Fig. 4) we have to expect that the same Δe should result in larger elongation of a weak (long) bond ΔR_w as compared to the elongation of a strong (short) bond ΔR_s. Thus $\Delta R_w > \Delta R_s$, which remains in agreement with the above-mentioned simple empirical observation of the highest dilatation along the longest bonds. An analogous approach may be used to compare the thermal expansions of isomorphous crystals where differentiation of bond energies results also from the different chemical composition, influencing the bond lengths, J-factors and $e–R$ slopes. A detailed example will be given in 2.2., Predictions, and in Table II.

The difference between the classical description of thermal expansion and one proposed in the present work can be briefly summarized as follows. The classical approach starts from the fact that atoms (ions) in crystals vibrate anharmonically in the potential energy wells. Knowing the potential function one can calculate the mean positions of atoms (mean distances) and their changes with temperature which accounts for the thermal expansion. The present approach starts directly from the empirical bond-energy–bond-length dependence, on the assumption of the equipartition of the energy consumed on heating. Thus, as compared to the classical approach, it omits the dynamic part (vibrations) of considerations and ambiguities linked with a mathematical shape and coefficients of the potential functions to be chosen.

1.3. The Aim of the Work

So far the above-outlined phenomenological idea has not been studied. Its evaluation requires gathering of a certain amount of experimental data and this is what has begun to be done in this work.

We searched for an object of our studies among crystals of a relatively low symmetry for which anisotropic effects can be expected. Preferentially, the chosen crystal should be a matrix of solid solutions in which isomorphous substitutions of ions of various valence states (or vacancies) are possible, which brings about significant changes in the bond energies. Our final choice was solid solutions in the matrices of the bivalent metal vanadates crystallizing in the brannerite-type structure. Investigation of their thermal expansion is the main topic of this work.

2. Materials Chosen for the Present Study and Preliminary Predictions on Their Thermal Properties

2.1. Materials

A number of bivalent metal vanadates MeV_2O_6 (*Me* = Mg, Mn, Co, Cu, Zn, Cd) crystallize in the monoclinic brannerite-type structure or at least one of the polymorphs exhibits this structure (*14*). In the brannerite-type structure (*14*) (Fig. 1) distorted VO_6 octahedra sharing edges and corners form the anionic sheets parallel to (001) plane and Me^{2+} cations situated also in the distorted octahedra (sharing edges and making isolated [010] pillars) link the anionic layers along [001]. Further details will be given later in this work. The same structure is adapted by $LVMoO_6$ compounds (*L* = Li, Na, Ag) (*16, 17*). In our earlier work (*18–26*) we have shown that some of the MeV_2O_6

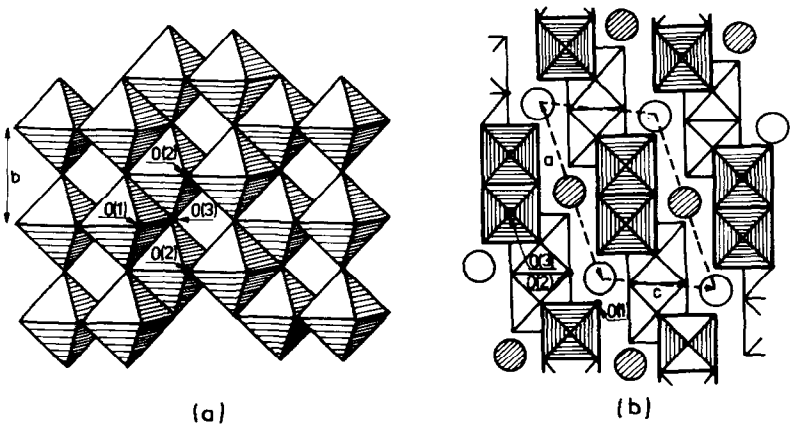

FIG. 1. Idealized presentation of the brannerite-type structure (after (*15*)). (a) A sheet of VO_6 octahedra parallel to the (001) plane. (b) Projection of the structure on the (010) plane with Me^{2+} cations and VO_6 octahedra at two levels, distinguished by slashing (see also Fig. 3).

compounds form the four-component solid solutions with MoO_3 and Li_2O of the general formula $Me_{1-x-y}\phi_x Li_y V_{2-2x-y}Mo_{2x+y}O_6$ (labeled $MeLi\phi$) in which Mo^{6+} ions are substituted randomly for V^{5+} and similarly Li^{1+} and cation vacancies ϕ for Me^{2+}. As $MeLi\phi = (1 - x - y)\ MeV_2O_6 + y\ LiVMoO_6 + 2x\ MoO_3$, it is convenient to represent the range of stability of $MeLi\phi$ using the equilateral composition triangle MeV_2O_6–LiV MoO_6–MoO_3 (Fig. 2), where composition variables $X = 100x$ and $Y = 100y$ are marked along the MeV_2O_6–MoO_3 and MeV_2O_6–$LiVMoO_6$ arms, respectively. The extreme cases of $MeLi\phi$ are:

$$Me\phi = Me_{1-x}\phi_x V_{2-2x}Mo_{2x}O_6 \text{ (at } y = 0),$$

$$MeLi = Me_{1-y}Li_y V_{2-y}Mo_y O_6 \text{ (at } x = 0),$$

$$Li\phi = Li_{1-x}\phi_x V_{1-x}Mo_{1+x}O_6 \text{ (at } x + y = 1).$$

$Li\phi$ exists in the range $0 \le X \le 16$ (*16*). $Me\phi$ are known for Me = Mn, $0 \le X \le 45$ (*18, 19, 21, 22*); Me = Co, $2 \le X \le 22$ (*23, 26*); and Me = Zn, $0 \le X \le 15$ (*24*). $MeLi$ have been found to exist for Me = Mn (*22*), Co (*26*), Zn (*24*), and Mg (*25*) in the whole composition range between MeV_2O_6 and LiV MoO_6, with the exception of a small range close to CoV_2O_6. $MeLi\phi$ are known for the same cations as $MeLi$ (*22, 24–26*) and their

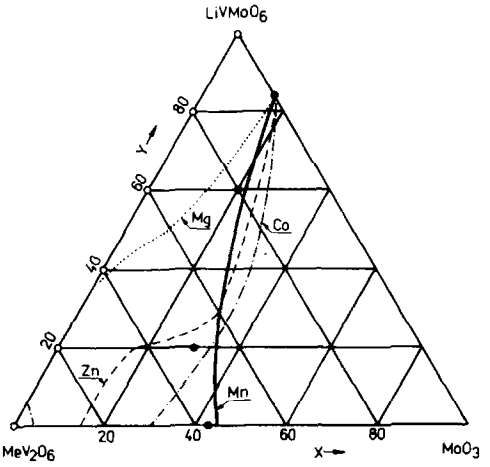

FIG. 2. Composition triangle MeV_2O_6–LiV MoO_6–MoO_3 in which the areas of stability of the solid solutions $MeLi\phi = Mn_{1-x-y}\phi_x Li_y V_{2-2x-y}Mo_{2x+y}O_6$ are marked for Me = Mn, Co, Zn, and Mg. These areas are located between MeV_2O_6, $LiVMoO_6$, and the respective bordering lines (with the exception of Me = Co close to CoV_2O_6). Open circles and solid circles indicate the composition of samples studied in this work and belonging to the MnLi (= MnLiϕ with x = 0) and MnLiϕ series, respectively.

stability ranges are strongly dependent on *Me* as shown in Fig. 2. Our long-time aim is to study the thermal expansion of all these phases.

In the present work we focus on a number of samples belonging to the MnLi and MnLiϕ types of the composition expressed further as MnLi-*X*-*Y* and MnLiϕ-*X*-*Y*. They include also the lateral matrices MnV_2O_6 and $LiVMoO_6$. The chosen samples form two series. The first involves MnLi–0–0 (= MnV_2O_6), MnLi–0–20, MnLi-0-40, MnLi-0-60, MnLi-0-80, and MnLi-0-100 (= $LiVMoO_6$). These samples belong to the MnV_2O_6–$LiVMoO_6$ system and contain no cation vacancies. They allow one to follow the influence of the Li/Mn and Mo/V substitutions on the thermal expansion of the matrix. The second series of samples comprises MnLiϕ–43–0 (= Mnϕ–43), MnLiϕ–30–20, MnLiϕ–20–60, MnLiϕ–16–84 (= Liϕ–16). These samples may be considered as the MnLi matrices of differentiated *Y*, saturated (or nearly) with cation vacancies (cf. Fig. 2), hence permitting the effect of ϕ's on the thermal expansion to be followed.

2.2. *Predictions*

As the effect of isomorphous substitutions in MnV_2O_6 on the thermal expansion is to be studied it seems relevant to recall (Table I) the *J* and *Jz* values for cations building up the system. The meaning of *J* [kcal $mol^{-1}vu^{-1}$] has been explained above (Eq. (13)). On the other hand *Jz* [kcal mol^{-1}] may be considered as the *entire binding ability of a cation* involving all the bonds around it and accounting for the local cohesion of the lattice. As can be calculated from Table I, the substitution of Mo^{6+} for V^{5+} increases the cohesion by 28%, Li^{1+} for Mn^{2+} decreases it by 36%, and ϕ for Mn^{2+} diminishes it to zero. The expected influence of doping on the thermal expansion is opposite to that on the cohesion. Let us call the indicated changes in cohesion and expansion the Mo/V, Li/Mn, and ϕ/Mn effects of substitution, respectively, or briefly the *Jz*-effects.

TABLE I

J-FACTORS [kcal mol^{-1} vu^{-1}] AND THE ENTIRE BINDING ABILITIES *Jz* [kcal mol^{-1}] OF CATIONS BUILDING THE MnLi AND MnLiϕ SOLID SOLUTIONS

Ion	*J*	*Jz*
V^{5+}	91.4	457.0
Mo^{6+}	85.9	515.4
Mn^{2+}	109.3	218.6
Li^{1+}	139.7	139.7
ϕ	0	0

More detailed considerations can be given for the pure MnV_2O_6 matrix. Although the atomic positions in MnV_2O_6 have never been determined, it has been pointed out (*21, 27*) that this structure can be successfully approximated by that of MgV_2O_6 (*28*) with minor corrections resulting from the difference between the ionic radii of Mg^{2+} and Mn^{2+} (*7*). The structure approximated in this way is shown in Fig. 3. Bond lengths *R*, strengths *s* (Eq. (12)) and energies *e* (Eq. (13)) are listed in Table II. As can be seen in Table II, the bond energies in MnV_2O_6 vary markedly (26–115 kcal mol^{-1}), which should account for differentiation of the individual expansions of the bonds. An example is included in Table II. Under the assumption of the energy equipartition, the energy of each bond is diminished by 1 kcal mol^{-1}, new bond lengths R_{-1} are calculated from Eqs. (12) and (13) and the increments $\Delta R\%$ are determined. Let us note that the expected heat capacity of MnV_2O_6 is close to 54 cal mol^{-1} deg^{-1} (there are 9 gram-atoms per 1 gram-molecle) and the above calculative procedure changes the molecular atomization enthalpy by 18 kcal mol^{-1} (there are 18 *N* bonds per mole). Thus the procedure is equivalent to "heating" one mole of crystal by over 333°C. Figure 4

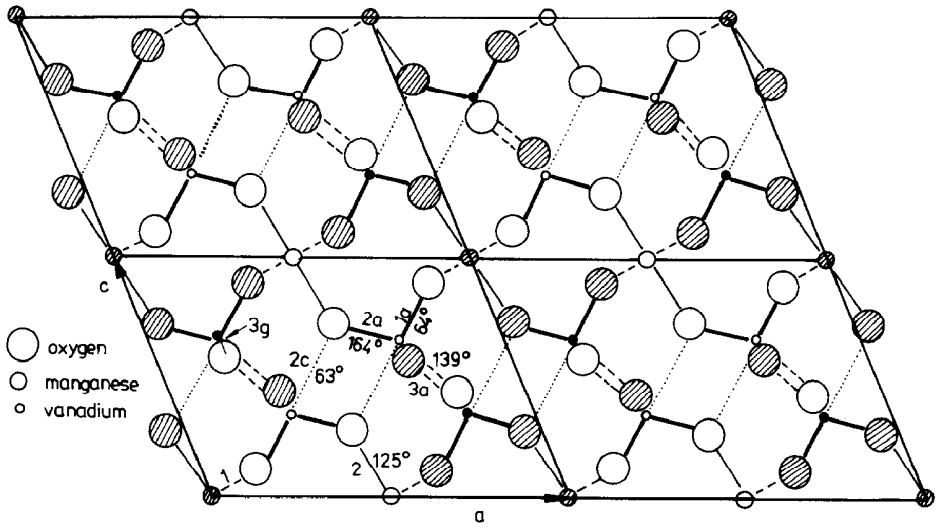

FIG. 3. Projection of the MnV_2O_6 structure on the (010) plane. Open circles represent atoms lying at $y = 0$, slashed or solid circles represent atoms lying at $y = 0.5\ b$. The bonds are classified according to their thermal sensitivities $\Delta R\%$ given in Table II: highly sensitive (dotted lines), moderately sensitive (dashed lines), weakly sensitive (solid lines), very weakly sensitive (thick solid lines). Numbers and letters are the symbols of the bonds and $\alpha_{b/[100]}$ angles that the bonds make with [100].

shows the $e - R$ curves resulting from Eqs. (12) and (13) for the V^{5+}–O, Mo^{6+}–O, Mn^{2+}–O, and Li^{1+}–O bonds. The curves have different positions along the energy axis and differ in the slope. Data gathered in Table II and Fig. 4 show that the expansibility of the bonds can be classified according to R, e, and $\Delta R\%$. If only the bonds of the given cation to oxygen are considered, all three classifications are equivalent. In accord with the old empirical rule mentioned in the paragraph 1.2., the longer the bond, the smaller e, the higher the $\Delta R\%$ increment at a given Δe. The rule does not work, however, when the bonds of various cations to oxygen are compared. R's be-

TABLE II

BOND LENGTHS R (Å), Strengths, s [vu], AND ENERGIES e [kcal mol^{-1}], IN MnV_2O_6 ALONG WITH NEW LENGTHS R_{-1} AND INCREMENTS $\Delta R\%$ CALCULATED FOR e DIMINISHED BY 1 kcal mol^{-1}

Bond	R	s	e	R_{-1}	$\Delta R\%$	Type of bond[a]
V–O(1*a*)	1.67	1.261	115.2	1.673	0.16	vws
V–O(2*a*)	1.67	1.261	115.2	1.673	0.16	vws
2 × V–O(3*g*)	1.85	0.783	71.6	1.857	0.36	ws
V–O(3*a*)	2.11	0.506	46.3	2.126	0.74	ms
V–O(2*c*)	2.67	0.287	26.3	2.719	1.83	hs
4 × Mn–O(1)	2.32	0.279	30.5	2.340	0.87	ms
2 × Mn–O(2)	2.14	0.398	43.5	2.150	0.45	ws

[a] *v*, very; w, weakly; m, moderately; h, highly; s, sensitive.

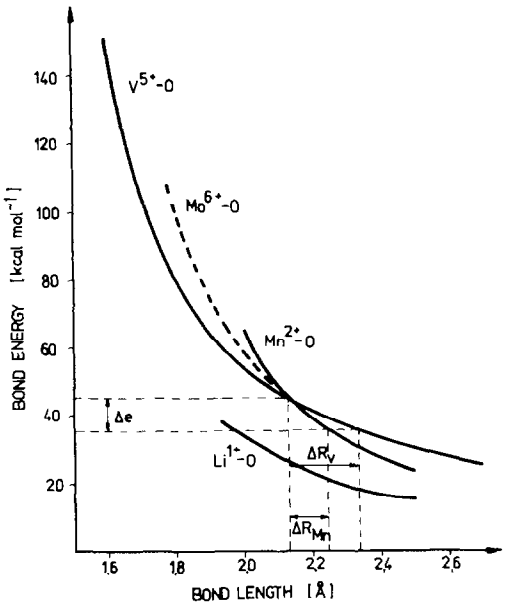

FIG. 4. The e–R curves for the V^{5+}–O, Mn^{2+}–O, Mo^{6+}–O, and Li^{1+}–O bonds (at higher R the curves for V^{5+}–O and Mo^{6+}–O nearly coincide, but the latter has a slightly higher slope). It can be seen that the same Δe gives, e.g., $\Delta R_V > \Delta R_{Mn}$, which is due to the different slopes of the curves. It can be easily deduced that the longer the initial R the higher ΔR at the same Δe.

come dependent on the individual ionic radii; e's depend on the individual values of J, d, z; $\Delta R\%$'s are sensitive moreover to the slope of the e–R curves. Thus neither R's nor e's but $\Delta R\%$ values (cf. Fig. 4) account directly for the individual thermal expansion of bonds. The latter ($\Delta R\%$) can thus be taken as a measure of the *thermal bond-length sensitivity*. The privileged role of $\Delta R\%$ values in the classification of bonds results from the e–R slope-effect.

On the basis of the $\Delta R\%$ values, four types of bonds may be distinguished in the considered structure (cf. Fig. 3):

—highly sensitive (hs)V–O(2c) bonds lying in the (010) plane and making an angle $\alpha^{\text{V–O(2}c\text{)}}_{b/[100]} = 63°$ with [100];

—moderately sensitive (ms) bonds of two kinds: (i) (ms)V–O(3a) bonds in the (010) plane of $\alpha^{\text{V–O(3}a\text{)}}_{b/[100]} = 139°$ (thus nearly perpendicular to (hs)), (ii) (ms)Mn–O(1) bonds inclined to the system of the crystallographic axes and axes of the tensor of thermal expansion (cf. the next section) and giving comparable projections on all these axes;

—weakly sensitive (ws) bonds of two kinds: (i) (ws)Mn–O(2) bonds in the (010) plane of $\alpha^{\text{Mn-O(2)}}_{b/[100]} = 125°$, (ii) (ws)V–O(3$g$) bonds nearly parallel to [010];

—very weakly sensitive (vws)V–O(1a) and (vws)V–O(2a) bonds in the (010) plane, with $\alpha^{\text{V–O(1a)}}_{b/[100]} = 64°$ and $\alpha^{\text{V–O(2a)}}_{b/[100]} = 164°$.

As the thermal bond-sensitvity (Table II) of the bonds listed above is about 22 : 10 : 5 : 2, mainly (vs) and (ms) bonds are expected to govern the thermal expansion and the highest expansion is expected along (hs)V–O(2c) nearly perpendicular to (201)—the plane of the easiest cleavage (*27*).

Unfortunately the local bond lengths are unknown for samples doped with Li and Mo. Therefore it is impossible to carry out so detailed an analysis as done above for MnV_2O_6. However, the slope effects can be considered qualitatively. In view of the higher slope of the e–R curve (Fig. 4) for the Mo–O bonds relative to the V–O bonds we can expect a decrease of the thermal bond-sensitivity after doping with Mo, in addition to the above-mentioned substitution effect related to Jz values. For the same reason the opposite changes are expected for Li–O replacing Mn–O.

We have to remember that the bonds in a crystal are not independent but make a tridimensional network. Therefore a "compromise" between the individual bond expansions and the network requirements may be expected. The above predictions and reservations will be compared below with the experimental results.

3. Experimental and Data Processing

All samples studied in this work were prepared by the amorphous citrate precursor method as described in detail in (*22*).

X-ray diffraction patterns were recorded every 50°C between room temperature and T_{max} of 535–660°C (close to the stability limit of the given phase, cf. Fig. 9) with a DRON-2 diffractometer using Cr$K\alpha$ radiation and a GPWT-1500 heating stage, controlled within ±0.5°C with a Pt/PtRh thermocouple. At room temperature Al (a = 4.0494 at 25°) was used as an internal standard. The patterns were indexed as described in (*22*) and lattice parameters were calculated from the positions of about 15 reflections.

A number of computer programs have been used for processing the data.

(i) The LATCON program from the CERN library, involving the least-squares method, was used to determine the unit cell parameters a, b, c, and β (which will be generally labeled below as "p").

(ii) The SMOOTH program was applied for smoothing the dependence of the lattice parameters on the temperature. It has been assumed that this dependence has a polynomial form,

$$p = \sum_{0}^{n} p_i T_i^n. \tag{15}$$

The p_i coefficients were determined and verified with the χ^2 test; n was usually found to be 2 and sometimes 1.

(iii) The TENSOR program served to determine the eigenvalues of the nondiagonal representation of the tensor of thermal expansion adequate for the monoclinic system

$$E = \begin{pmatrix} e_{11} & 0 & e_{13} \\ 0 & e_{22} & 0 \\ e_{31} & 0 & e_{33} \end{pmatrix} \tag{16}$$

First the thermal expansion of our monoclinic crystals was described in the orthogonal system of axes in which **X**′ was equivalent to [100], **Y**′ to [010], and **Z**′ ⊥ (001), as shown in Fig. 5, where the third crystallographic axis [001] is also marked. At a chosen temperature T_i (i = initial) the size of the unit cell may be described by three vectors $\mathbf{a}_i$, $\mathbf{b}_i$, and $\mathbf{c}_i$. After heating to T_f (f = final) they increase by $\Delta\mathbf{a}$, $\Delta\mathbf{b}$, and $\Delta\mathbf{c}$ and become $\mathbf{a}_f$, $\mathbf{b}_f$, and $\mathbf{c}_f$ with a simultaneous change of β_i to β_f (Fig. 5). The increments of the unit cell dimensions may be described as

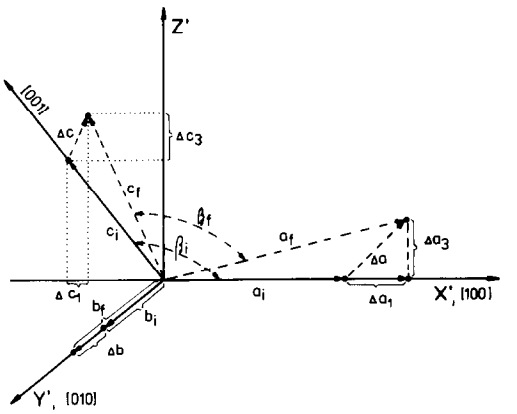

FIG. 5. Mutual situation of the system of axes in which the thermal expansion of the studied samples is described. [100], [010], [001] are the crystallographic axes. X', Y', Z' make the preliminary system of the orthogonal axes (nondiagonal tensor). Initial (i) and final (f) sizes of the unit cell and their increments (Δ) correspond to heating the crystal from T_i to T_f. The final system of the main orthogonal axes X, Y, Z (diagonal tensor) is shown in Fig. 6.

$$\begin{pmatrix} \Delta a_1 \\ 0 \\ \Delta a_3 \end{pmatrix} = \Delta T\, E \begin{pmatrix} a_i \\ 0 \\ 0 \end{pmatrix} \tag{17a}$$

$$\begin{pmatrix} 0 \\ \Delta b \\ 0 \end{pmatrix} = \Delta T\, E \begin{pmatrix} 0 \\ b_i \\ 0 \end{pmatrix} \tag{17b}$$

$$\begin{pmatrix} \Delta c_1 \\ 0 \\ \Delta c_3 \end{pmatrix} = \Delta T\, E \begin{pmatrix} c_i \cos\beta_i \\ 0 \\ c_i \cos\beta_i \end{pmatrix} \tag{17c}$$

where Δa_1, Δc_1, Δa_3, Δc_3 are the components of $\Delta\mathbf{a}$ and $\Delta\mathbf{c}$ parallel to [100] and [001], respectively, and $\Delta T = T_f - T_i$, ($\Delta T = 0.1$°C was used in all the numerical calculations). Equations (17a, 17b, and 17c) give a set of five equations of the first order which was solved with Cramer's determinants method. Numerical calculations were done with TENSOR. SMOOTH was then used to obtain the dependence of all the e_{ij} values on the temperature in an analytical form.

(iv) The DIAG program was used to diagonalize the E-tensor to the D-tensor,

$$D = \begin{pmatrix} d_{11} & 0 & 0 \\ 0 & d_{22} & 0 \\ 0 & 0 & d_{33} \end{pmatrix} \qquad (18)$$

This was a routine diagonalizing program including EISRG1 from the MATHSCI library. The obtained d_{11}, d_{22}, and d_{33} are the coefficients of the linear thermal expansion along three main orthogonal axes **X**, **Y**, and **Z** (Fig. 6), respectively, **Y** coinciding with **Y'** and **X** and **Z** making angles α_x and α_z with the **X'** (= [100]) axis, so that

$$\alpha_z = \alpha_x + 90°. \qquad (19)$$

The estimated accuracy of d_{ii} is 0.1×10^{-5}.

The volume thermal expansion d_V has been calculated as

$$d_V = d_{11} + d_{22} + d_{33}. \qquad (20)$$

Knowing d_{11}, d_{22}, and d_{33}, one can easily calculate the coefficients of thermal expansion d_r in a chosen direction inclined at angles α_r, β_r, and γ_r to the main axes

$$d_r = d_{11}\cos^2\alpha_r + d_{22}\cos^2\beta_r + d_{33}\cos^2\gamma_r. \qquad (21)$$

The points of all $\mathbf{d}_r$ vectors obtained on changing α_r, β_r, and γ_r continuously between 0 and 360° determine an ellypsoid of thermal expansion in the XYZ space.

(v) The FIG program (routine one) served to draw the bidimensional sections of the ellypsoids of the thermal expansion.

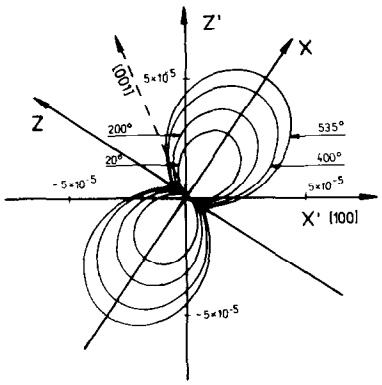

FIG. 6. Thermal expansion of the studied samples is finally described in the system of the main orthogonal axes X, Y, Z (diagonal tensor). Y = [010], X is inclined to the crystallographic [100] axis at α_x, which depends on the composition and temperature (54–82°C). XZ sections of the ellypsoids of thermal expansion of MnV_2O_6 at four temperatures are included.

4. Results and Discussion

Thermal expansion has been studied for six samples belonging to the MnLi series and four samples belonging to the MnLiϕ series, between room temperature and the decomposition temperature of 535–660°C.

The determined coefficients d_{11}, d_{22}, and d_{33} of the linear thermal expansion along three main orthogonal axes and α_x angles between the main X axis and the [100] crystallographic axis are listed in Tables III and IV. For clarity the d_{ii} and α_x values obtained at 20 and 500°C are also represented graphically in Fig. 7, as a function of the composition. The analogous plots for the volume thermal expansion d_V are shown in Fig. 8. Typical (010) = XZ sections of the ellypsoids of thermal expansion are given in Fig. 6.

Because of the extensive data processing, the original and intermediate results are not available to the reader. To give at least a sample of these results, lattice constants of MnV_2O_6 as a function of the temperature are given in Table V.

TABLE III

COEFFICIENTS OF THERMAL EXPANSION $d_{ii} \cdot 10^5$ and α_x ANGLES [deg] FOR THE MnLi SERIES OF SAMPLES, AS A FUNCTION OF TEMPERATURE

Sample	T[°C]	d_{11}	d_{22}	d_{33}	α_x
MnLi–0–0	20	3.16	0.46	0.23	56.36
(MnV_2O_6)	50	3.33	0.46	0.27	56.32
	100	3.61	0.46	0.33	56.25
	150	3.90	0.46	0.39	56.18
	200	4.18	0.46	0.46	56.12
	250	4.46	0.46	0.52	56.05
	300	4.74	0.46	0.58	55.98
	350	5.02	0.46	0.64	55.91
	400	5.29	0.46	0.69	55.84
	450	5.57	0.46	0.75	55.76
	500	5.84	0.46	0.81	55.69
	535	6.03	0.46	0.85	55.63
MnLi–0–20	20	2.88	0.32	0.41	54.16
	50	3.01	0.32	0.46	54.75
	100	3.22	0.32	0.53	55.64
	150	3.43	0.32	0.61	56.44
	200	3.64	0.32	0.68	57.16
	250	3.85	0.32	0.75	57.80
	300	4.06	0.32	0.82	58.38
	350	4.27	0.32	0.89	58.91
	400	4.48	0.32	0.96	59.38
	450	4.69	0.32	1.02	59.81
	500	4.90	0.32	1.09	60.19
	550	5.11	0.32	1.15	60.54
	600	5.32	0.32	1.22	60.86
	660	5.57	0.32	1.29	61.20
MnLi–0–40	20	2.85	0.32	0.57	56.63
	50	2.97	0.32	0.63	57.25
	100	3.16	0.32	0.73	58.23
	150	3.35	0.32	0.82	59.12
	200	3.55	0.32	0.92	59.94
	250	3.74	0.32	1.01	60.68
	300	3.93	0.32	1.10	61.37
	350	4.13	0.32	1.19	62.00
	400	4.33	0.32	1.27	62.57
	450	4.52	0.32	1.36	63.10
	500	4.72	0.32	1.45	63.58
	550	4.91	0.32	1.53	64.03
	600	5.11	0.32	1.61	64.44
	645	5.28	0.32	1.69	64.78
MnLi–0–60	20	3.14	0.26	0.69	60.10
	50	3.23	0.26	0.76	60.73
	100	3.39	0.26	0.87	61.74
	150	3.54	0.26	0.98	62.71
	200	3.69	0.26	1.08	63.64
	250	3.85	0.26	1.19	64.53
	300	4.00	0.26	1.29	65.37
	350	4.16	0.26	1.39	66.18
	400	4.32	0.26	1.49	66.94
	450	4.48	0.26	1.58	67.67
	500	4.63	0.26	1.68	68.35
	550	4.79	0.26	1.77	69.01
	600	4.95	0.26	1.87	69.62
	655	5.12	0.26	1.97	70.26
MnLi–0–80	20	2.83	0.26	0.85	63.04
	50	2.98	0.26	0.92	64.19
	100	3.24	0.26	1.03	65.90
	150	3.49	0.26	1.14	67.40
	200	3.75	0.26	1.24	68.70
	250	4.01	0.26	1.35	69.83
	300	4.27	0.26	1.45	70.83
	350	4.53	0.26	1.55	71.70
	400	4.79	0.26	1.65	72.45
	450	5.05	0.26	1.74	73.15
	500	5.31	0.26	1.84	73.75
	550	5.57	0.26	1.93	74.28
	600	5.85	0.26	2.02	74.76
	645	6.06	0.26	2.10	75.14
MnLi–0–100	20	3.62	0.20	1.13	63.30
($LiVMoO_6$)	50	3.85	0.20	1.26	65.53
	100	4.14	0.20	1.40	68.05
	150	4.44	0.20	1.54	70.27
	200	4.75	0.20	1.66	72.22
	250	5.06	0.20	1.78	73.93
	300	5.37	0.20	1.89	75.43
	350	5.69	0.20	2.00	76.78
	400	6.01	0.20	2.10	77.89
	450	6.33	0.20	2.20	78.90
	500	6.64	0.20	2.30	79.80
	550	6.96	0.20	2.39	80.59
	570	7.09	0.20	2.42	80.89
	600	7.28	0.20	2.48	81.30
	630	7.47	0.20	2.53	81.68

Let us begin the interpretation with the MnLi series and in particular with the d_V composition dependence (Fig. 8). The d_V–Y curves pass through a minimum at Y of about 20–30, which means that at this composition the lattice shows the highest cohesion. The minimum of d_V coincides with the maximum of the thermal stability of MnLi at $Y = 25$, resulting from the MnV_2O_6–$LiVMoO_6$ phase diagram determined formerly (*22*) and recalled in Fig. 9. It follows from Table I that along the MnLi series we deal with two Jz effects. Substitution of Mo^{6+} for V^{5+} should increase the cohesion and decrease the thermal expansion; substitution of Li^{1+} for Mn^{2+} should result in the opposite changes. The curves d_V–Y show that the Mo/V effect prevails for $Y < 25$ and the Li/Mn one for $Y > 25$. Further comments concerning the existence of these two ranges will be given below when analyzing the d_{11} composition dependence.

TABLE IV

COEFFICIENTS OF THERMAL EXPANSION $d_{ii} \cdot 10^5$ and α_x ANGLES [deg] FOR THE MnLi SERIES OF SAMPLES, AS A FUNCTION OF TEMPERATURE

Sample	T[°C]	d_{11}	d_{22}	d_{33}	α_x
MnLiϕ-43-0	20	2.68	0.54	0.33	62.91
	50	2.81	0.54	0.41	63.19
	100	3.02	0.54	0.55	63.61
	150	3.24	0.54	0.69	64.01
	200	3.45	0.54	0.84	64.37
	250	3.66	0.54	0.98	64.71
	300	3.87	0.54	1.11	65.03
	350	4.08	0.54	1.25	65.32
	400	4.29	0.54	1.39	65.60
	450	4.50	0.54	1.52	65.85
	500	4.71	0.54	1.66	66.08
	550	4.92	0.54	1.80	66.23
	570	5.00	0.54	1.85	66.38
MnLiϕ-30-20	20	2.74	0.20	0.76	64.29
	50	2.86	0.20	0.83	64.65
	100	3.07	0.20	0.93	65.20
	150	3.27	0.20	1.03	65.69
	200	3.48	0.20	1.14	66.13
	250	3.68	0.20	1.24	66.52
	300	3.88	0.20	1.34	66.88
	350	4.09	0.20	1.44	67.20
	400	4.29	0.20	1.54	67.48
	450	4.49	0.20	1.64	67.74
	500	4.70	0.29	1.73	67.97
	550	4.90	0.20	1.83	68.18
	600	5.10	0.20	1.93	68.38
MnLiϕ-20-60	20	3.40	0.16	0.97	73.53
	50	3.52	0.16	1.04	73.60
	100	3.71	0.16	1.16	73.69
	150	3.89	0.16	1.28	73.77
	200	4.06	0.16	1.40	73.84
	250	4.26	0.16	1.52	73.90
	300	4.44	0.16	1.64	73.95
	350	4.62	0.16	1.75	73.99
	400	4.81	0.16	1.87	74.03
	450	4.99	0.16	1.98	74.05
	500	5.17	0.16	2.10	74.07
	550	5.34	0.16	2.21	74.08
	600	5.52	0.16	2.33	74.08
	615	5.58	0.16	2.36	74.09
MnLiϕ-16-84	20	3.91	0.19	1.27	68.06
	50	4.11	0.19	1.36	69.45
	100	4.37	0.19	1.48	71.04
	150	4.63	0.19	1.59	72.45
	200	4.90	0.19	1.70	73.72
	250	5.16	0.19	1.80	74.85
	300	5.42	0.19	1.90	75.86
	350	5.69	0.19	2.00	76.76
	400	5.96	0.19	2.09	77.57
	450	6.22	0.19	2.18	78.30
	500	6.49	0.19	2.27	78.95
	550	6.75	0.19	2.36	79.55
	600	7.01	0.19	2.45	80.08
	630	7.17	0.19	2.50	80.38

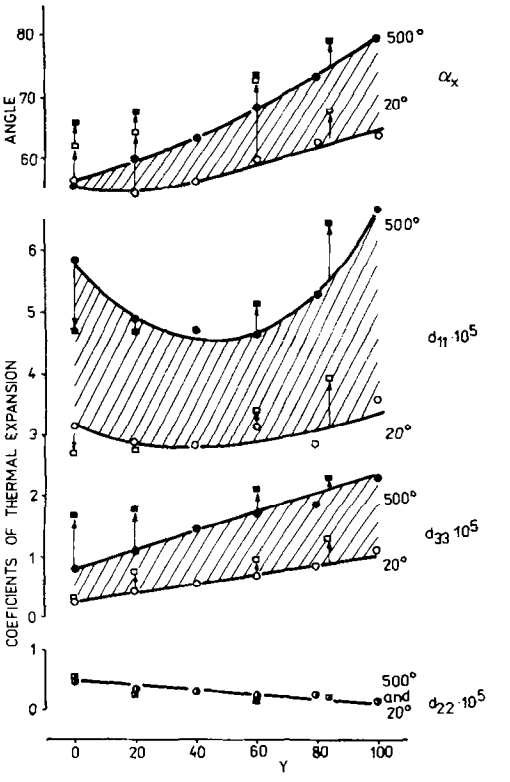

FIG. 7. Coefficients of the linear thermal expansion d_{11}, d_{22}, d_{33} along three main orthogonal axes and the α_x angle as a function of composition, at 20 and 500°C. Circles and lines refer to the MnLi series with Y being the composition variable. Squares refer to the MnLiϕ series; arrows show the changes of d_{ii} related to the insertion of cation vacancies (in quantities indicated in Table IV) to the MnLi-matrix at a given Y.

The value of d_V is the resultant of d_{11}, d_{22}, and d_{33}. The coefficients d_{ii} are also sensitive to composition but in different ways. The values of d_{11}, which are always the highest, pass through a minimum at $Y \approx 40$, behaving thus similarly to d_V and showing sensitivity to both the Mo/V and the Li/Mn substitution effects. The α_x angles essentially increase with Y (and temperature) from 54 to 82°C. Both the highest values of d_{11} (among d_{ii}) and the values obtained for α_x remain in very good agreement with the prediction that the highest expansion should take place

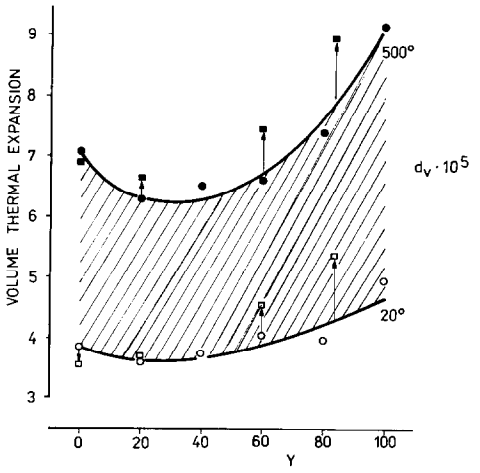

FIG. 8. Coefficient of the volume thermal expansion d_V as a function of the composition of the MnLi and MnLiϕ solid solutions at 20 and 500°C. The meaning of circles and squares is the same as in Fig. 7.

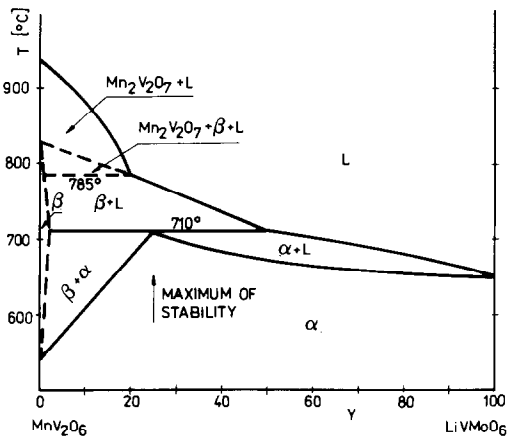

FIG. 9. The phase diagram of the MnV_2O_6–$LiVMoO_6$ system (after (*22*)), α, MnLi (brannerite-type); β, high temperature modification of MnLi; L, liquid.

along (vs)V–O(2*c*) bond of $\alpha \frac{\text{V–O}(2c)}{b/[100]} =$ 63°C, although the (ms)Mn–O(1) bond (or its projection on the direction close to [101]) should also give an impact into dilatation. Thus indeed d_{11} could be sensitive to both the Mo/V and Li/Mn Jz effects. Let us note that the Mn–O(1) bonds make bridges between the anionic layers, O(1) being common for two adjacent Mn atoms,

TABLE V

LATTICE CONSTANTS OF MnV_2O_6 AS A FUNCTION OF TEMPERATURE (δ_T IS AN ANGLE BETWEEN [100] AXES AT ROOM TEMPERATURE AND AT A GIVEN TEMPERATURE T; cf. FIG. 5.)

T [°C]	a [Å]	b [Å]	c [Å]	β [deg]	δ_T [deg]
20	9.3097	3.5340	6.7530	112.58	0.00
50	9.3131	3.5345	6.7554	112.53	0.02
100	9.3192	3.5353	6.7599	112.45	0.07
150	9.3258	3.5361	6.7647	112.36	0.11
200	9.3331	3.5369	6.7700	112.26	0.16
250	9.3409	3.5377	6.7757	112.16	0.21
300	9.3494	3.5385	6.7818	112.05	0.26
350	9.3584	3.5393	6.7884	111.93	0.32
400	9.3680	3.5401	6.7954	111.81	0.38
450	9.3782	3.5409	6.8028	111.68	0.45
500	9.3889	3.5418	6.8106	111.55	0.51
535	9.3968	3.5423	6.8164	111.45	0.56
Maximal standard deviation	0.0028	0.0015	0.0022	0.014	

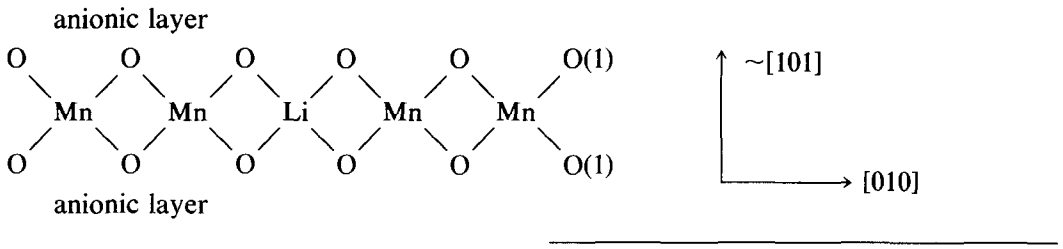

Substitution of Li^{1+} for Mn^{2+} increases the thermal sensitivity of these bonds, which should give rise to the increase of d_{11} along the MnLiϕ series as the Jz effect for Li/Mn (−38%) is stronger than that for Mo/V (+28%). However, at low Li concentration the atoms of lithium are isolated and "clathrated" between the stronger Mn–O(1) bonds, which can suppress the expansion of the Li–O(1) bonds. More precisely, we should speak about elongation of the Li–O bonds according to the energy equipartition, but with local angular bond–bond rotation, without any noticable change of the Li–O bond projections on the direction close to [101]. At lower Y the negative influence of the Mo/V Jz effect on expansion can thus prevail. At higher Y, the Li atoms may appear in the adjacent positions, cancelling the Mn–O(1) clathration, and Li influence may become dominant. Apparently the same accounts for the minimum in the d_V composition dependence.

Values of d_{33} are much smaller as compared to d_{11} and usually much higher than d_{22} (with the exceptions of MnLi–0–0 and MnLiϕ–43–0 at very low temperatures, where the differences are comparable to the experimental error). According to Table II and Fig. 3, d_{33} is to be ascribed to the (ms)V–O(3a) bonds (nearly perpendicular to (vs)V–O(2c)) with some impact from the (ws)Mn–O(2) bonds. The linear increase of d_{33} with increasing Y reveals that the d_{33} composition dependence is governed mainly by Li/Mn (in (ws)Mn–O(2)) and must be ascribed to the slope effect, more pronounced for a Li–Mn pair than for a Mo–V pair. Let us note that the O(2) atoms are not shared by the adjacent Mn atoms and therefore the above-described clathrate effect does not operate here.

There are only two bonds which can influence d_{22}, which usually has the smallest value. These are the (ms)Mn–O(1) and (ws)V–O(3g) bonds, which change on doping into Li–O and Mo–O, respectively. As d_{22} is the smallest and diminishes with increasing Y, it must be ruled by the Mo/V substitution effect. We have thus to conclude that d_{22} is governed mainly by the (ws)V–O(3g) bonds, making infinite chains along the crystal and hindering the increase of the projection of (ms)Li/Mn–O(1) on [010]. This observation together with the behavior of d_{11} indicates that the Li–O(1) bonds are doubly clathrated by the (ms)Mn–O(1) and (ws)V/Mo–O(3g) bonds. However, they still have a step of freedom consisting in angular changes around [010]. Perhaps another possibility for the consumption of the equipartitioned energy lies in an increase of the vibration energy.

Let us pass to the MnLiϕ series of samples. The squares in Figs. 7 and 8 represent the results obtained for the MnLiϕ samples and arrows show the changes of d_{ii} related to the insertion of cation vacancies to the MnLi matrix at a given Y. According to intuition and Table I, the incorporation of vacancies should decrease the cohesion and increase the thermal expansion. This is indeed observed in all the cases, with the exceptions of d_{11} and d_V of MnLiϕ–43–0 and d_{11} of MnLiϕ–30–20, where a decrease of the expansion, in spite of the insertion of

ϕ's, markedly exceeds the experimental error. This unexpected phenomenon is to be ascribed to the clathrate effect of ϕ's (like that of Li atoms) by the (ms)Mn–O(1) bonds.

5. Conclusions

The ancient empirical rule that the highest dilatation of a crystal corresponds to the direction of the longest bonds has been the starting point of this work.

On the basis of the obtained results, as well as the bond-length–bond-energy concept and the assumption of the energy equipartition some more precise rules can be formulated. We are putting them forward, being conscious that they require further verification and perhaps some amelioration.

(i) Thermal Bond-Sensitivity Rule

Individual thermal expansion of a bond is governed by the thermal bond-length sensitivity $\Delta R\%$ (related to Δe) which depends on the initial bond length R and on the slope of the e–R curve of a given cation–anion pair. The higher the initial R and the milder the slope, the higher the expansion (cf. Table II, values of R_{-1} and $\Delta R\%$).

(ii) Isomorphous Substitution Rule

In the case of the isomorphous doping the changes of thermal expansion of a crystal can be deduced from the entire binding abilities, Jz, of a mother atom and a dopant and from the slopes of their e–R curves. The lower Jz and the milder the slope, the higher the expansion. (cf. Table I and Fig. 4).

(iii) Weak Link Rule

If alternating stronger and weaker bonds make chains along or close to a given direction the thermal expansion of a crystal is governed predominantly by $\Delta R\%$ of the weaker bonds and their orientation (cf. Fig. 3, sequence of bonds close to [102]; Fig. 7, d_{11} has the highest value; α_x is close to $\alpha_{b/[100]}^{(\mathrm{hs})\mathrm{V}-\mathrm{O}(2c)}$).

(iv) Strong Chain Rule

If stronger and weaker bonds make the independent parallel chains along or close to a given direction the thermal expansion of a crystal in this direction is governed by $\Delta R\%$ of the stronger bonds. The weaker bonds can respect the energy equipartition but with angular changes (cf. Fig. 7; d_{22} is governed by (ws)V–O($3g$) bonds and not by (ms)Mn–O(1)).

(v) Clathrate Rule

If isolated weaker bonds are "immersed" inside the network of stronger bonds, the latter control the thermal expansion of a crystal and either local angular bond–bond reorganization of the weaker bonds takes place or the portion of the equipartited energy is used, e.g., to increase the vibrational energy instead of lengthening the bonds (cf. Figs. 7 and 8; d_{11} and d_V at small Y in the MnLi series and in the presence of cation vacancies; d_{22} in whole the range of Y and X; double clathrating of the Li–O(1) bonds).

The present approach has been already compared in the above text with the classical description of the thermal expansion. It has been pointed out that the empirical bond-energy–bond-length relation is used now (where the bond length means an average interatomic distance). Due to this fact the dynamic part of considerations (vibrations) is omitted. In this way we bypass the ambiguities concerning the choice of the mathematical shape of the potential function of interatomic interactions and numerical coefficients which enter it.

References

1. R. S. KRISHAN, E. SRINIVASAN, AND S. DEVANARAYANAN, "Thermal Expansion of Crystals," Pergamon Press (1979).

2. R. M. HAZEN AND L. W. FINGER, "Comparative Crystal Chemistry; Temperature, Pressure, Composition and the Variation of Crystal Structure," Wiley, New York (1984).
3. C. KITTEL, "Introduction to Solid State Physics," Wiley, New York (1968).
4. L. PAULING, *J. Amer. Chem. Soc.* **51,** 1010 (1923).
5. I. D. BROWN, *in* "Structure and Bonding in Crystals" (M. O'Keeffe and A. Navrotsky, Eds.), Vol. 2, Academic Press, New York (1981).
6. I. D. BROWN, *Phys. Chem. Miner.* **15,** 30 (1987).
7. J. ZIÓŁKOWSKI, *J. Solid State Chem.* **57,** 269 (1985).
8. J. ZIÓŁKOWSKI AND L. DZIEMBAJ, *J. Solid State Chem.* **57,** 291 (1985).
9. J. ZIÓŁKOWSKI, *J. Solid State Chem.* **61,** 343 (1986).
10. R. D. SHANNON, *Acta Crystallogr. Sect. A* **32,** 751 (1976).
11. J. ZIÓŁKOWSKI, *J. Catal.* **100,** 45 (1986) and papers quoted therein.
12. J. ZIÓŁKOWSKI, *Surface Sci.* **209,** 536 (1989).
13. J. ZIÓŁKOWSKI, E. BORDES, AND P. COURTINE, *J. Catal.* **122,** 126 (1990).
14. K. MOCAŁA AND J. ZIÓŁKOWSKI, *J. Solid State Chem.* **71,** 522 (1987) and papers quoted therein.
15. R. RUH AND A. D. WADSLEY, *Acta Crystallogr.* **21,** 974 (1966).
16. J. GALY, J. DARRIET, AND B. DARRIET, *C.R. Acad. Sci. Paris Ser. C* **264,** 1477 (1967).
17. B. DARRIET AND J. GALY, *Bull. Soc. Fr. Mineral. Cristallogr.* **91,** 325 (1968).
18. R. KOZŁOWSKI, J. ZIÓŁKOWSKI, K. MOCAŁA, AND J. HABER, *J. Solid State Chem.* **35,** 1 (1980); Erratum **38,** 138 (1981).
19. J. ZIÓŁKOWSKI, R. KOZŁOWSKI, K. MOCAŁA, AND J. HABER, *J. Solid State Chem.* **35,** 297 (1980).
20. T. MACHEJ, R. KOZŁOWSKI, AND J. ZIÓŁKOWSKI, *J. Solid State Chem.* **38,** 97 (1981).
21. R. KOZŁOWSKI AND K. STADNICKA, *J. Solid State Chem.* **39,** 271 (1981).
22. J. ZIÓŁKOWSKI, K. KRUPA, AND K. MOCAŁA, *J. Solid State Chem.* **48,** 376 (1983).
23. K. MOCAŁA, J. ZIÓŁKOWSKI, AND L. DZIEMBAJ, *J. Solid State Chem.* **56,** 84 (1985).
24. K. MOCAŁA AND J. ZIÓŁKOWSKI, *J. Solid State Chem.* **71,** 426 (1987).
25. K. MOCAŁA AND J. ZIÓŁKOWSKI, *J. Solid State Chem.* **71,** 552 (1987).
26. B. MASŁOWSKA AND J. ZIÓŁKOWSKI, *J. Solid State Chem.* **87,** 208 (1990).
27. J. ZIÓŁKOWSKI, *J. Catal.* **81,** 311 (1983).
28. H. N. NG AND C. CALVO, *Canad. J. Chem.* **50,** 3619 (1972).